PNAS Nexus, 2024, 3, pgae219
https://doi.org/10.1093/pnasnexus/pgae219
Advance access publication 6 June 2024
Research Report

Watching the Grand Ethiopian Renaissance Dam from a distance: Implications for sustainable water management of the Nile water

Karem Abdelmohsen[a,b,c], Mohamed Sultan[a,*], Eugene Yan[d], Abotalib Z. Abotalib[a,e], Himanshu Save[f], Mustafa Emil[a], Hesham Elhaddad[a,c] and Karim Abdelmalik[g]

[a]Geological and Environmental Sciences, Western Michigan University, Kalamazoo, MI 49008, USA
[b]School of Sustainability, Arizona State University, Tempe, AZ 82581, USA
[c]Geodynamics Department, National Research Institute of Astronomy and Geophysics, Cairo 11421, Egypt
[d]Environmental Science Division, Argonne National Laboratory, Lemont, IL 60439, USA
[e]Geology Department, National Authority for Remote Sensing and Space Sciences, Cairo, Egypt
[f]Center for Space Research, The University of Texas at Austin, TX 78759-5321, USA
[g]Geology Department, Faculty of Science, Ain Shams University, Cairo 11566, Egypt
*To whom correspondence should be addressed: Email: mohamed.sultan@wmich.edu
Edited By: Barbara Romanowicz

Abstract

Increased demands for sustainable water and energy resources in densely populated basins have led to the construction of dams, which impound waters in artificial reservoirs. In many cases, scarce field data led to the development of models that underestimated the seepage losses from reservoirs and ignored the role of extensive fault networks as preferred pathways for groundwater flow. We adopt an integrated approach (remote sensing, hydrologic modeling, and field observations) to assess the magnitude and nature of seepage from such systems using the Grand Ethiopian Renaissance Dam (GERD), Africa's largest hydropower project, as a test site. The dam was constructed on the Blue Nile within steep, highly fractured, and weathered terrain in the western Ethiopian Highlands. The GERD Gravity Recovery and Climate Experiment Terrestrial Water Storage ($GRACE_{TWS}$), seasonal peak difference product, reveals significant mass accumulation (43 ± 5 BCM) in the reservoir and seepage in its surroundings with progressive south-southwest mass migration along mapped structures between 2019 and 2022. Seepage, but not a decrease in inflow or increase in outflow, could explain, at least in part, the observed drop in the reservoir's water level and volume following each of the three fillings. Using mass balance calculations and $GRACE_{TWS}$ observations, we estimate significant seepage (19.8 ± 6 BCM) comparable to the reservoir's impounded waters (19.9 ± 1.2 BCM). Investigating and addressing the seepage from the GERD will ensure sustainable development and promote regional cooperation; overlooking the seepage would compromise hydrological modeling efforts on the Nile Basin and misinform ongoing negotiations on the Nile water management.

Keywords: climate variability, GRACE and GRACE-FO, water mass balance, sustainable management

Significance Statement

This research addresses the pressing issue of sustainable water and energy resources, particularly concerning the commonly overlooked or underestimated seepage from artificial reservoirs in areas where field data are scarce. In our assessment of the nature and magnitude of seepage from artificial reservoirs in highly fractured terrains (e.g. the Grand Ethiopian Renaissance Dam [GERD]), we compensated for data scarcity by employing an innovative integration of Gravity Recovery and Climate Experiment satellite observations, mass balance calculations, and field data. By revealing substantial seepage influenced by underlying geologic structures, our findings challenge prevailing assumptions and contribute vital insights to the Nile Basin negotiations.

Introduction

The Nile River Basin covers approximately 10% of African territory (area: 2,870,000 km^2) in Burundi, the Democratic Republic of the Congo, Egypt, Eritrea, Ethiopia, Kenya, Rwanda, South Sudan, Sudan, Tanzania, and Uganda, with a total population exceeding 300 million (1). The bulk of the Nile Basin runoff comes from precipitation over the source areas of the White and Blue Niles in equatorial Africa and the Ethiopian Highlands, respectively (2); however, the exploitation of the Nile water occurs mainly in the downstream hyper-arid riparian countries (i.e. Egypt and

Competing Interest: The authors declare no competing interests.
Received: December 21, 2023. **Accepted:** May 21, 2024

Sudan). For example, Egypt, the most populous country in North Africa (>100 million), receives more than 97% of its freshwater supplies from the Nile River streamflow, over 85% of which originates in the Ethiopian Highlands and is channeled by the Blue Nile, Sobat, and Atbara rivers (2, 3).

In April 2011, the Ethiopian government began constructing the Grand Ethiopian Renaissance Dam (GERD) on the Blue Nile, some 45 km from the Ethiopian–Sudanese borders. The GERD and its reservoir upstream capture the runoff from the Blue Nile subbasin that extends over large sections of the northwestern Ethiopian Plateau (176,000 km^2)(4). Upon completion, it will be the largest hydropower dam in Africa. The completion of construction of the dam's main base in July 2020 allowed reservoir filling to start in that year (5). The first filling was reported as being completed on 2020 August 14, the second on 2021 August 9, and the third on 2022 August 12, where the targeted volumes were 4.9, 13.5, and 22 BCM, respectively (6). When the reservoir reaches its total capacity, the lake water level (WL) will be at 640 m.a.m.s.l, cover 1,904 km^2, and impound 74 BCM of water (7).

Unsurprisingly, the construction of the GERD has caused tensions between Ethiopia and the downstream countries (Egypt and Sudan) (8). Numerous studies have been conducted to examine the filling strategies of GERD (6, 9, 10) and their socioeconomic (11, 12) and environmental impacts (13, 14), as well as the hazards associated with the construction of the new mega-dam (15, 16). Other studies focused on developing stochastic hydrological models to predict the river behavior during and after the GERD's filling (17–19). Regardless of whether the filling will be expedited in the upcoming years or not and whether the filling will be painful or tolerable to the downstream countries under average or extended drought periods, we believe that the timetable for filling the GERD and the prevalent climatic conditions during the filling years should not be the only primary concerns of the downstream countries. After all, many of these problems will end with the completion of the filling of the GERD reservoir. Instead, they should be more concerned about the potential losses to seepage and, to a lesser extent, evaporation. Those will last after filling the reservoir.

The GERD will control the water flow downstream, facilitating agricultural expansion in Sudan and raising additional concerns regarding the long-term impacts on water allocations in the Nile Basin. While the evaporation losses can be estimated with a high degree of certainty (~1.7 BCM/year) (6, 8, 9, 20), the seepage losses will vary depending largely on the local geology of the area (Section 1 in the Supplementary file). The evaporation from the Nile Basin reservoirs is a dynamic parameter that will differ from year to year depending on the totality of the system's operation. The evaporation from the GERD reservoir will increase as its surface area increases. In contrast, the surface area and losses to evaporation in the Aswan High Dam reservoir will decline with reduced flow, lowering the overall evaporation in the system (10). The long-term impacts of evaporation losses and agricultural expansion on the water management plans in the Nile Basin are acknowledged in the modeling efforts of the Nile River water dynamics (6, 11). On the other hand, the seepage losses that could represent a major component of the GERD water balance are largely overlooked in all previous modeling efforts of the Nile flow dynamics under GERD construction.

To address this deficiency, we first show that the geologic and hydrogeologic setting of the study area promotes seepage from the GERD reservoir and then apply an integrated approach that utilizes field observations, temporal Gravity Recovery and Climate Experiment (GRACE) and GRACE-Follow-on (GRACE-FO) observations, Sentinel-1 radar data, and radar altimetry, and mass balance calculations from measured outflow, estimated inflow, and reservoir volume to assess the magnitude and nature of seepage from the GERD reservoir. Such estimates are needed to achieve sustainable management scenarios of the Nile waters between upstream and downstream countries.

The Blue Nile watershed is bound by the uplifted western flank of the Main Ethiopian Rift in the east and southeast and by the uplifted sides of the Melut Rift in the west (Fig. 1).

The Blue Nile River main stream runs northward within the Blue Nile Rift (22). The Neoproterozoic basement block over which the GERD and the reservoir were built is the site of complex and multistage tectonic, erosional, and depositional events that left their imprints on the geomorphologic, lithologic, and structural settings of the area (Section 2 in the Supplementary file). The extended and recurrent tectonic activities in Western Ethiopia left behind a highly deformed landscape decorated by a fractured faulted and folded terrain network (23, 24), including the GERD and its reservoir sites (Figs. 1, 2).

Upon completing the filling of the reservoir, it will extend over Precambrian metamorphic rocks and syn-, late-, and post-tectonic intrusive (Section 2 in the Supplementary file), calcite, and dolomite, and Tertiary basalts (25, 27). The outcrops to be covered by the final filling of the reservoir are hereafter referred to as reservoir rock units (RRU) (Fig. 2). The basement rocks of Western Ethiopia, including the RRU, have better groundwater storage capabilities yet lower conductance than the basement rocks in all other parts of Ethiopia (28). The high conductance is attributed to the high precipitation rates (up to an annual average of 1,800 mm) (29) that promote recharge, the thick regolith (up to 60 m) that facilitates storage, and the undulating topography that promotes aggregation of weathering products in the lowlands (28, 30) (Section 3 in the Supplementary file). The above-reported high storage potentiality in Western Ethiopia, together with the dense network of fractures and faults, raises a concern about the extent of seepage from the RRU and justifies a detailed examination. We assessed reservoir seepage using radar altimetry measurements upstream and downstream, mass balance calculations, and temporal variations in $GRACE_{TWS}$ over the reservoir and its surroundings.

Results

In this section, we investigate the magnitude and nature of the seepage from GERD in view of the reservoir's water budget from Sentinel-1 and radar altimetry, the reservoir's flux estimates and mass balance calculations, and large-scale water storage variations from GRACE and GRACE-FO. We provide evidence in support of significant losses from GERD.

Water budget of the reservoir from Sentinel-1 and radar altimetry

The Sentinel-1 radar data were used to map the temporal variations in the areal extent of the GERD reservoir throughout the filling years. Radar penetrates clouds, operates in bright and dark settings, and effectively delineates water bodies that appear as dark areas on these images since they reflect radar waves away from the sensor. Knowing the areal extent of the reservoir and its topography (from digital elevation models [DEMs]), we estimated the volume of water in the reservoir. Temporal Sentinel-1 radar images (Fig. 3) show the extension of the Blue Nile River before the initiation of the first filling (Fig. 3a) and the areal extent of the reservoir following the first (Fig. 3b), second (Fig. 3c), and third fillings (Fig. 3d). The surface water elevations and volumes of

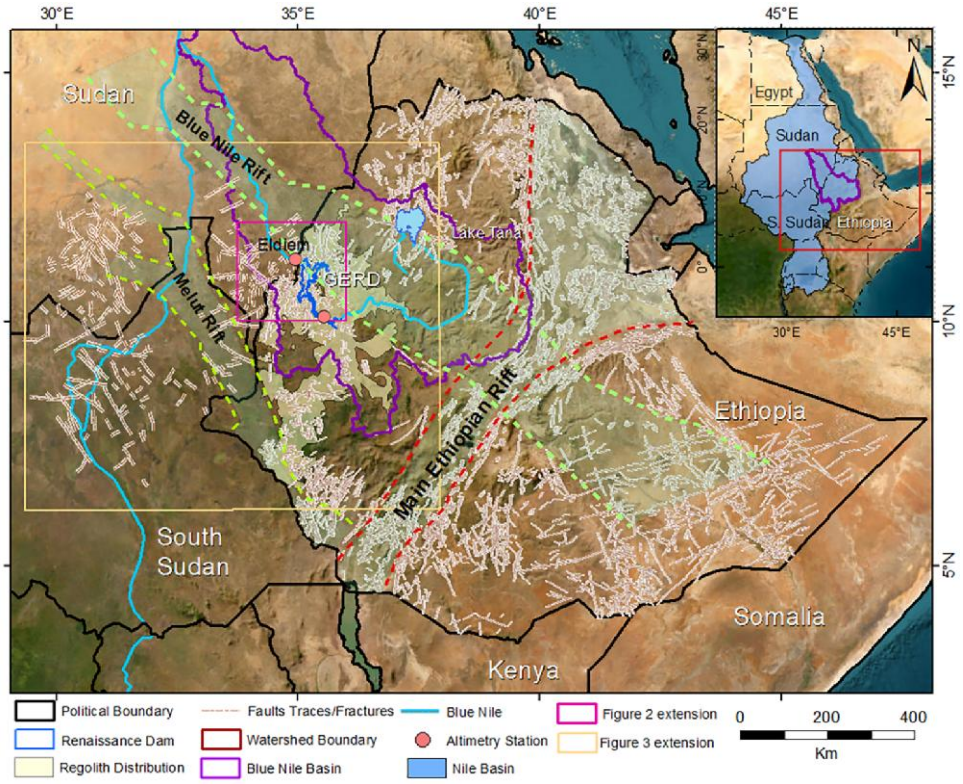

Fig. 1. Location map of the GERD some 45 km from the Ethiopian–Sudanese borders. The map shows the location and extension of the GERD reservoir upon completion, the downstream Eldiem stream flow gauge station (latitude 11.239896° N; longitude 34.950073° E), and the altimetry stations upstream (latitude 10.0751° N; longitude 35.5325° E) and downstream (Eldiem stream flow gauge station location) of the GERD. Also shown are the Blue Nile River, Lake Tana, the Blue Nile subbasin, the distribution of faults across the country, and their extension in neighboring Sudan (white lines) (21), the Main Ethiopian Rift Valley, the Mesozoic extensional basins (outlined by dashed green lines) (22). The inset shows the distribution of the Nile Basin and the Blue Nile subbasin. Background is a false color Landsat image Service Layer Credits: Source: Esri, Maxar, Earthstar Geographics, and the GIS User Community.

impounded waters in the reservoir extracted from Sentinel-1 time series and a DEM (refer to Sections 'Sentinel-1 radar images and radar altimetry' and 'Mass balance calculations') are displayed in Figure 4. The onset of the first filling was captured in an image acquired on 2020 July 1 (Fig. 3a), from which the WL and water volume (WV) were estimated at 538 m.a.m.s.l. and 0.58 ± 0.03 BCM, respectively. The WL and WV for the first filling were extracted from a radar image acquired on 2020 August 14 (WL, 566 m.a.m.s.l.; WV, 4.3 ± 0.2 BCM), the second filling from an image acquired on 2021 August 9 (WL, 580 m.a.m.s.l.; WV, 9.3 ± 0.1 BCM), and the third filling from an image acquired on 2022 September 21 (WL, 606 m.a.m.s.l.; WV, 26.8 ± 1.5 BCM).

During the filling phases (fillings I, II, and III), we observed a significant decrease in the GERD WV and WL after each filling in the summers of 2020, 2021, and 2022, respectively. This pattern is observed during those three-year dry months (January–June). We also observe a progressive increase in the loss in reservoir volumes following each filling period (Fig. 4, Table 1).

The drop in WL and WV following each filling period could be attributed to one or more anthropogenic or natural factors: evaporation, decrease in inflow or increase in outflow (release of impounded waters from the dam), and seepage from the lake to the surroundings. The reservoir extended over a relatively small area in years I, II, and III (<850 km^2). Thus, the total losses to evaporation during years I, II, and III are limited (<3.5 ± 0.9 BCM) and cannot account for the observed reservoir losses (12 ± 0.7 BCM; Table 1) during the same period.

Using radar altimetry measurements, we tested whether the decline in WL and WV following each filling period in years I, II, and III was related to an increase in outflow or a decrease in inflow by examining the temporal variations in surface WLs upstream and downstream of the GERD. Radar altimetry measures the two-way travel time of a radar pulse between the satellite antenna and the Earth's surface at the nadir. The pulse is reflected by the water surface and received by the sensor onboard the satellite. We identified the closest two locations to the dam where radar altimetry data are available over the mainstream. We then used the observed temporal variations in surface WLs in the upstream and downstream locations to proxy the variations in reservoir inflow and outflow, respectively. Examination of Figure 4 reveals that during the months when the WLs declined (October–June), the inflow remained constant, and the outflow decreased. A similar pattern is observed for the outflow at Eldiem station; a decrease in outflow occurs during the periods when a drop in WL and WV occurs in each of years I, II, and III (Fig. 4). These observations suggest that the reduction in the WL is unlikely caused by an increase in outflow or a decrease in inflow and more likely by losses to reservoir seepage.

Reservoir's flux estimates and mass balance calculations

In the upstream country (Ethiopia), the stream gauging station data are not publicly available, making it necessary to use alternative methods to estimate the inflow rate. We applied two methods to derive upstream inflow rates (refer to Section 'Extraction of temporal variations in the inflow to and outflow from the GERD during the filling years'). In the first method, we

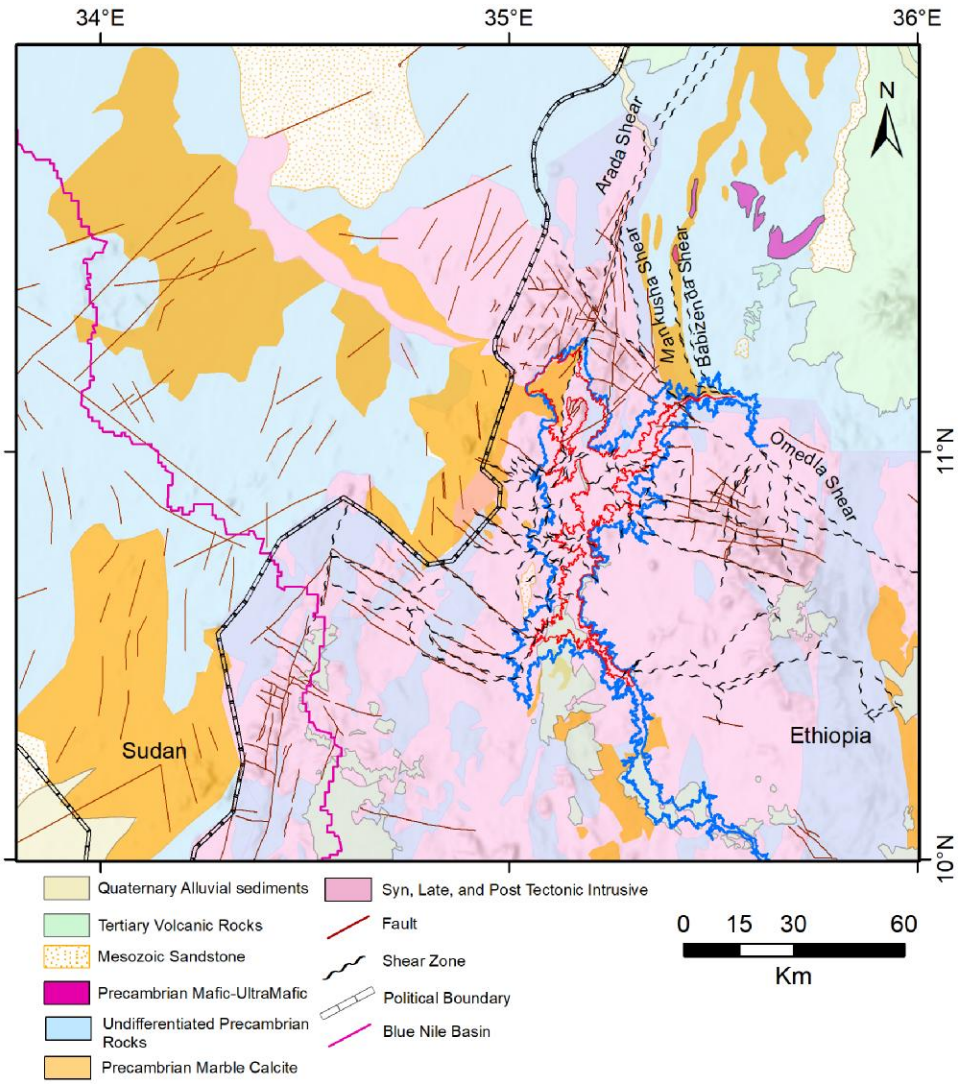

Fig. 2. A simplified geologic map of the study area. The map covers the GERD and its reservoir and displays the region's lithologic and structural setting (faults and shear zones) (25, 26). Also shown is the GERD reservoir's areal extent after the third filling (WL, 606 m.a.m.s.l; area, 841 km^2, storage, 26.8 ± 1.5 BCM; polygon outlined by red line; Table 1). Upon completion of the filling, the WL will reach 640 m.a.m.s.l, its area will extend over 2,107 km^2, and its storage will reach 74 BCM (polygon outlined by blue line; Table 1).

used the Manning's equation. This empirical equation describes the relationship between the velocity in a channel and the channel geometry, slope, and friction coefficient expressed as a Manning *n*. In this application, we extracted surface WLs from radar altimetry data and measured river cross-sectional area using a 2.5-m DEM dataset at the upstream location. We calibrated Manning's equation by adjusting the parameters and shapes of the open channel against the observed streamflow, assuming that inflow is equal to outflow before filling the GERD. The calibration was optimized using criteria of both Nash–Sutcliffe efficiency (NSE) and Kling–Gupta efficiency (KGE) scores, and the calibrated Manning's equation (NSE = 0.903 and KGE = 0.929) was used to estimate inflow at the upstream location using WLs derived from radar altimetry after the filling started. The first method is hereafter referred to as Manning's equation application. In the second method, we also assumed the inflow was equal to the outflow at Eldiem station before filling the GERD (2009–2019), derived a relationship (NSE, 0.83; root mean square error [RMSE], 0.1) between the surface water elevation upstream (from radar altimetry) and measured downstream outflow (Eldiem station). We then used the relationship to estimate the inflow rate during the GERD operational period. Finally, we used each of the two inflow rate estimates to derive daily losses to seepage or gain from base flow following the GERD construction (Fig. 5).

The positive and negative values in Figure 5 indicate losses and gains from the system. The former (losses) are assumed to be related to seepage and the latter (gains) to base flow. During years I, II, and III, losses and gains are observed throughout the year. The losses exceed the gains and are observed mainly during the wet rainy season, as infiltration and seepage will increase with the increase in the reservoir surface WLs and area. We estimated the losses to seepage from 2019 to 2022 at 18.4 ± 2.5 BCM from the first method (Manning's application method) and 18 ± 1.8 BCM from the second method (Fig. 5). The estimated seepage from Manning's equation should be considered as a minimum value given that the Beles River intersects the main channel downstream of the altimetry station where the inflow was estimated. Thus, its contributions were not included in the estimated inflow.

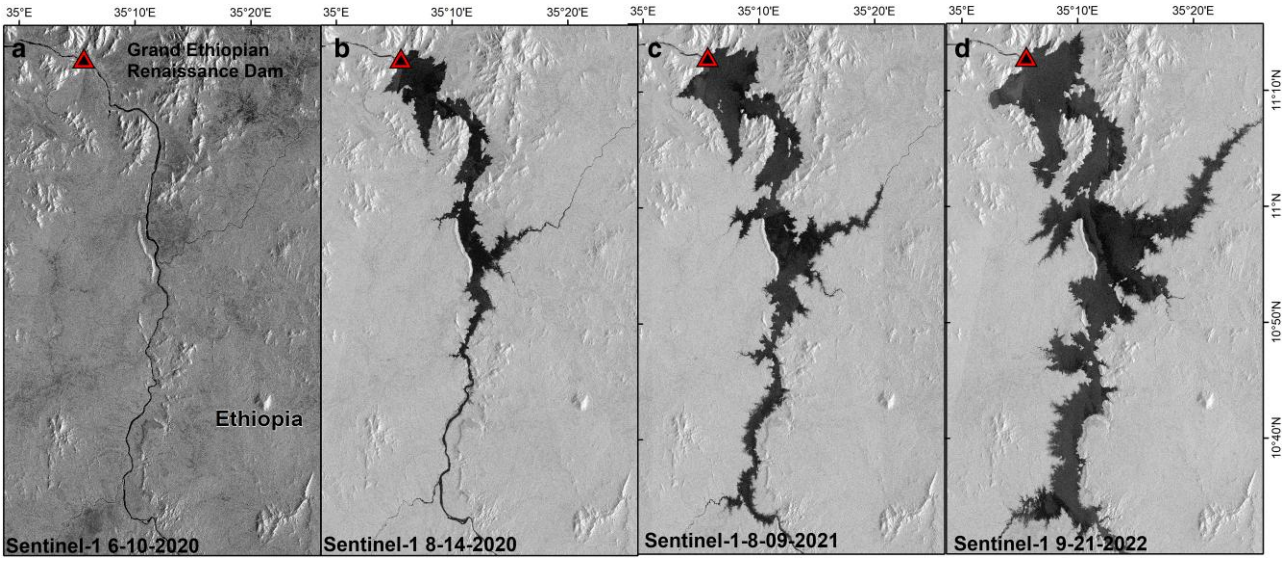

Fig. 3. Areal extent of the GERD reservoir during fillings I, II, and III from Sentinel-1 images. Sentinel-1 radar images over the GERD and its reservoir showing the distribution of the Blue Nile before the construction of the GERD (2020 June 10; river width: 300–500 m; a) and the areal extent of the reservoir after the completion of the first filling (2020 August 14; area: 207 km^2;b), the second filling (2021 August 9; area: 379 km^2;c), and the third filling (2022 September 21; area: 841 km^2, d).

Large-scale water storage variations from GRACE and GRACE-FO

The GRACE was designed to map the temporal variations in the Earth's global gravity field and to estimate the variations in terrestrial water storage (TWS) on a monthly basis (32). We extracted a $GRACE_{TWS}$ product displaying the spatial and temporal increase in $GRACE_{TWS}$ over the GERD and its surroundings throughout the years of the reservoir filling. The product, hereafter referred to as $GRACE_{TWS}$ seasonal peak difference product, was constructed by subtracting the seasonal peak (annual maximum) of $GRACE_{TWS}$ of 2019 from that of 2022 (Fig. 6a). A three-dimensional (3D) representation of the seasonal peak difference product is shown in Figure 3b. 2019 is the year preceding the construction of the GERD, and 2022 is the third year of filling.

The seepage estimates from Methods I and II are similar to the losses (23 ± 5 BCM) extracted from the cumulative increase of $GRACE_{TWS}$ (43 ± 5 BCM; Fig. 5b) less the water impounded in the reservoir in December 2022 (19.9 ± 1.2 BCM; Table 1). We report the seepage losses as the average of the three estimates (19.8 ± 6 BCM), the GRACE-based seepage, and the two estimates from the mass balance calculations; the uncertainty (6 BCM) was calculated by adding, in quadrature, the individual errors from each of the three methods. Reporting the seepage from the average of the three estimates allows for a more comprehensive inclusion of potential errors uncounted for in the inflow estimates.

We also investigated whether the $GRACE_{TWS}$ seasonal difference product revealed migration patterns of infiltrated waters from the reservoir. We suspected that water impoundment in the GERD reservoir would lead to a progressive increase in $GRACE_{TWS}$ over the GERD reservoir and its surroundings throughout fillings I, II, and III, with the maximum $GRACE_{TWS}$ values in the summer of 2022. The difference product should portray the mass accumulation following the dam construction within the reservoir and possibly away from it from seepage. Figure 6a and b shows significant mass accumulation (>20 cm). Areas with mass accumulation between 20 to 21 cm are represented by warm tones, while areas with mass accumulation between 22 to 24 cm are indicated by even warmer tones. The figure shows an anomaly extending for some 300 km from the Ethiopian Highlands construction site in a southwest direction toward the lowlands in South Sudan. We defined the areal extent for the GRACE anomaly statistically and visually (Fig. 6); it is the polygon encompassing all contiguous pixels whose values exceed the mean (10 cm) by 1 SD (9 cm). The anomaly shows a cumulative increase of $GRACE_{TWS}$ amounting to 43 ± 5 BCM centered over an area between the Ethiopian Highlands and the White Nile.

One interpretation of the observed anomaly is that it indicates seepage from the reservoir and groundwater flow along preferred pathways to the lowlands in the south. If this were the case, one would expect the anomaly to originate from the GERD reservoir and to overlap with the distribution of fault networks that presumably channeled the infiltrated waters from the highlands to the lowlands. The inspection of Figure 6 shows that this is the case. The anomaly starts from the dam site; its extension follows the distribution of the fault network in the highlands and its projected extension under the sand cover, suggesting that those systems could have acted as preferred pathways for groundwater flow (Fig. 6). A similar conceptual model was proposed for Lake Nasser, where the model calls on seepage from Lake Nasser and rapid groundwater flow along a network of faults, fractures, and karst topography for hundreds of km in 3 to 5 months. The model was supported by the analysis of the seasonal $GRACE_{TWS}$, distribution of fault and fracture networks, the stable isotopic compositions of groundwater, and monitoring well data (33).

Alternatively, the anomaly could be caused by temporal (2019–2022) variations in precipitation intensity and patterns over the anomaly or variations in the runoff from the highlands. We compared the TWS time series over the anomaly from two sources, the GRACE and GRACE-FO and the Global Land Data Simulation System (GLDAS) model (Fig. 7). The former ($GRACE_{TWS}$) measures the natural and anthropogenic contributions, whereas the latter estimates the natural contributions only. The figure shows a general correspondence between the two datasets before dam construction (2002–2019) and a significant deviation following the dam construction (2020–2022). If natural factors caused the anomaly, one should expect to observe a good correspondence between the $GLDAS_{TWS}$ and $GRACE_{TWS}$ values between 2019 and 2022.

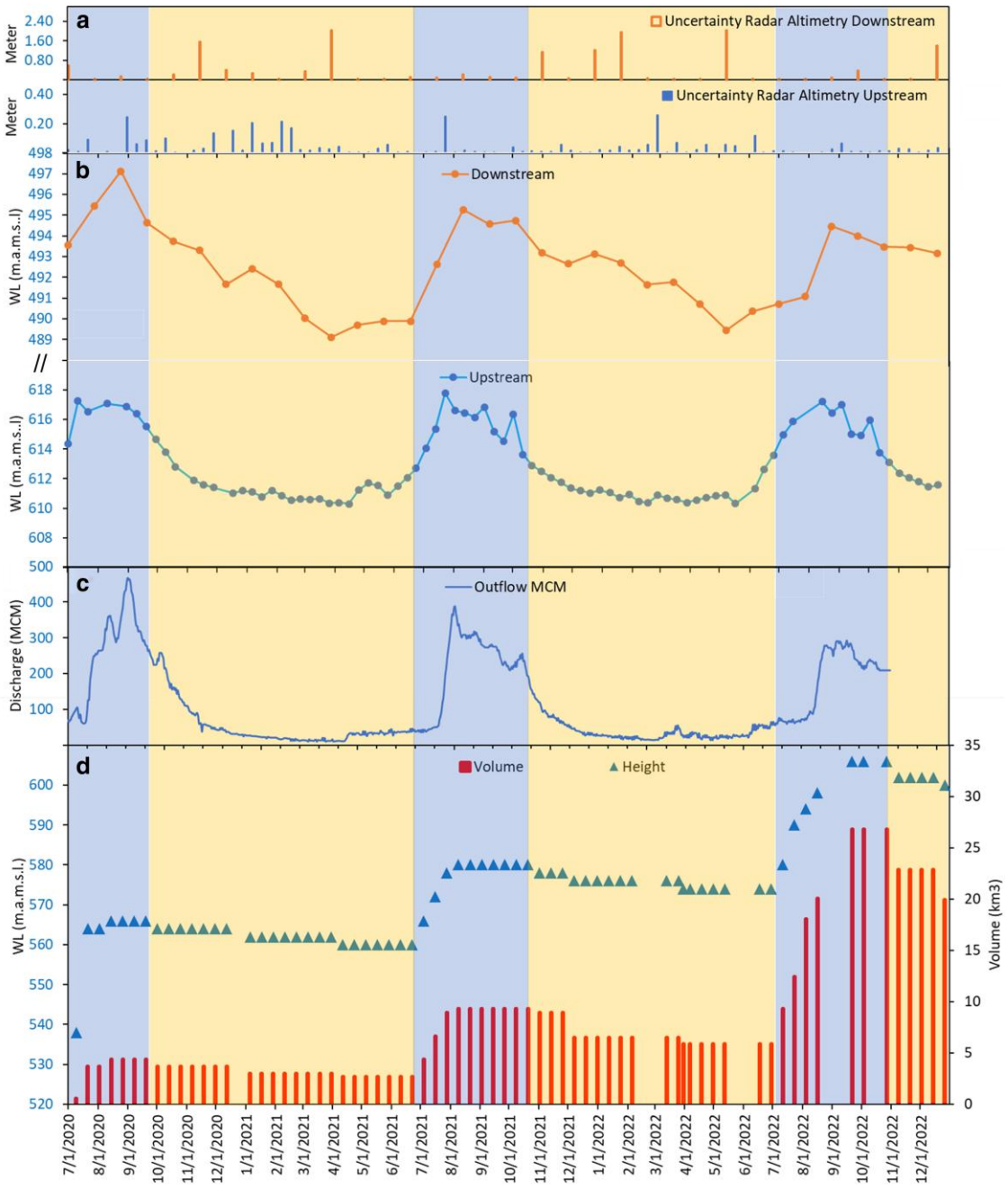

Fig. 4. Comparison between WVs and surface WLs in the reservoir and in its upstream and downstream stations, and at the Eldiem outflow station. a) The uncertainty in radar altimetry elevations reported by the DAHITI. b) Radar altimetry elevation over the upstream (latitude 10.0751° N; longitude 35.5325° E; Figs. 1, 6) and the Eldiem station (latitude 11.239896° N; longitude 34.950073° E; Figs. 1, 6). c) Measured outflow at Eldiem station. d) Temporal lake storage (red bars), rising and stable WLs (triangles in blue-shaded periods), and declining WLs (triangles in yellow-shaded periods).

The observed progressive deviation between the two times series following dam construction supports the earlier model (seepage from the GERD reservoir) but not the latter (variation in precipitation). Also, if variations in precipitation intensity and patterns between 2020 and 2022 caused the observed anomaly, one would expect a progressive increase in rainfall over the anomaly area during the filling period corresponding to the observed rise in $GRACE_{TWS}$. Figure 7 shows that this is not the case. The $GRACE_{TWS}$ showed a progressive increase from 2019 to 2022, whereas the intensity of the annual precipitation (AP) increased in 2020 but gradually declined from 2020 to 2022 [AP: 2019, 1,027 mm; 2020, 1,204 mm; 2021, 1,193 mm, 2022, 1,105 mm (Fig. 7a and b)]. In Section 4 in the Supplementary file, we present observations that argue against the anomaly being related to variations in runoff from the Ethiopian Highlands.

Monitoring well data is needed to verify the advocated seepage in areas surrounding the GERD reservoir, where the groundwater levels are expected to rise along the preferred pathways for groundwater flow. Although monitoring well data is unavailable to test whether groundwater levels within the anomaly area rose following the GERD's construction, another line of evidence suggests this. Inspection of satellite imagery over the anomaly area revealed that previously unobserved (2002–2019) marshes began developing in 2020 in the lowlands proximal to and east

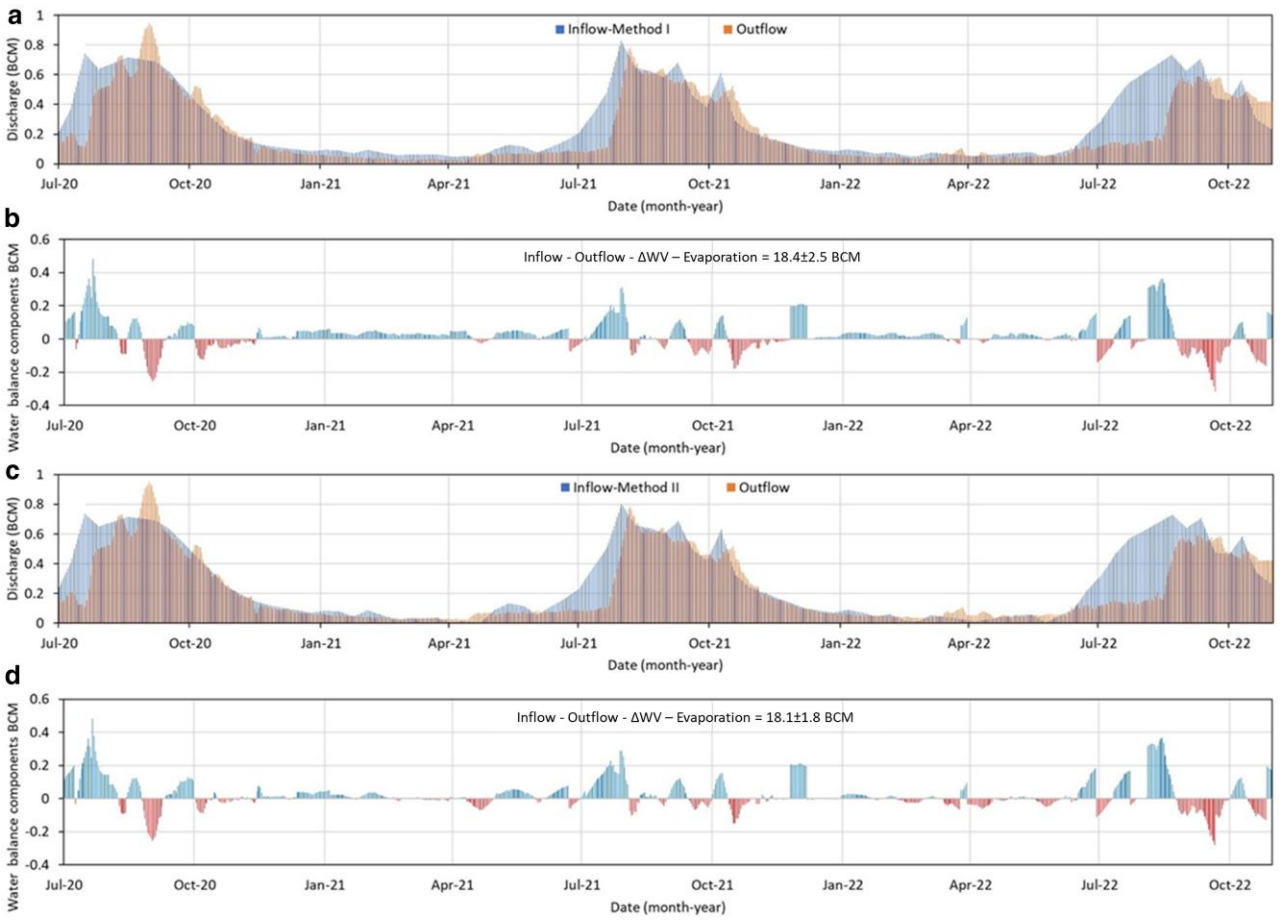

Fig. 5. Daily inflow (a, c) and mass balance calculations (b, d) using Methods I and II. a) Comparison of observed outflow and estimated inflow (Method I), calculated from radar altimetry data, river cross-sectional area, and applying Manning's equation (refer to Section 'Extraction of temporal variations in the inflow to and outflow from the GERD during the filling years'). b) Estimated daily losses to seepage (postive values) or gain to base flow (negative values) using the inflow values represented in a) and applying the mass balance calculations (refer to Section 5.4.3). c) Comparison of observed outflow data and estimated inflow (Method II), using a relationship between the upstream radar altimetry-based surface water elevation and measured outflow (refer to Section 'Extraction of temporal variations in the inflow to and outflow from the GERD during the filling years'). d) Estimated daily losses to seepage (postive values) or gain to base flow (negative values) using inflow values represented in c) and applying procedures described in Section 'Estimating losses to seepage using mass balance calculations'.

of the Nile Valley. Because the marshes progressively increased in size from 109 km^2 in 2020 to 328 km^2 in 2022, whereas precipitation decreased during the same period (2020 to 2022), the marshes are more likely to have formed by groundwater flow originating from the reservoir and discharging in the lowlands and less likely to be related to precipitation (Section 5 in the Supplementary file).

Discussion and limitations

The geologic and hydrogeologic setting of the study area raises concerns about the extent of seepage from the GERD reservoir. It is a highly fractured area that witnessed multiple extensional episodes that left behind a complex network of shear systems, faults, and fractures and is characterized by thick regolith and deep weathering profiles. Seepage from and away from the reservoir could be through laminar flow within the regolith and turbulent flow along fault networks (32). We provided three main pieces of evidence suggesting that seepage from the GERD reservoir could result in significant losses from the system and thus impede the achievement of sustainable water management of the Nile flow. The first relates to the observed decline in WL and WV following each filling period that could not be accounted for by evaporation, a decrease in inflow, or an increase in outflow, leaving seepage-related losses as the most plausible explanation.

The second line of evidence comes from the losses estimated from the water mass balance (WMB) calculations (18 ± 1.8; 18.4 ± 2.5 BCM), similar to the losses extracted from the $GRACE_{TWS}$ difference product (23 ± 5 BCM). The estimated losses up to the third filling stage are significant, amounting to the retained waters in the reservoir. To date, the surface water elevations have increased by some 70 m and over 130 m upon completion of reservoir filling. This high gradient and the terrain's geologic and structural setting could explain the estimated high seepage rates. Similar high seepage rates were reported from artificial reservoirs elsewhere (Section 1 in the Supplementary file).

The third line of evidence comes from the $GRACE_{TWS}$ seasonal peak difference product. It shows significant mass accumulation in the reservoir and its surroundings following the dam construction but none in the preceding years. There is a progressive south-southwest mass migration from the highlands toward the lowlands in South Sudan (second piece of evidence). The identified path for groundwater flow follows the distribution of faults and shear systems in the highlands and their projected extension under the sand cover in Sudan.

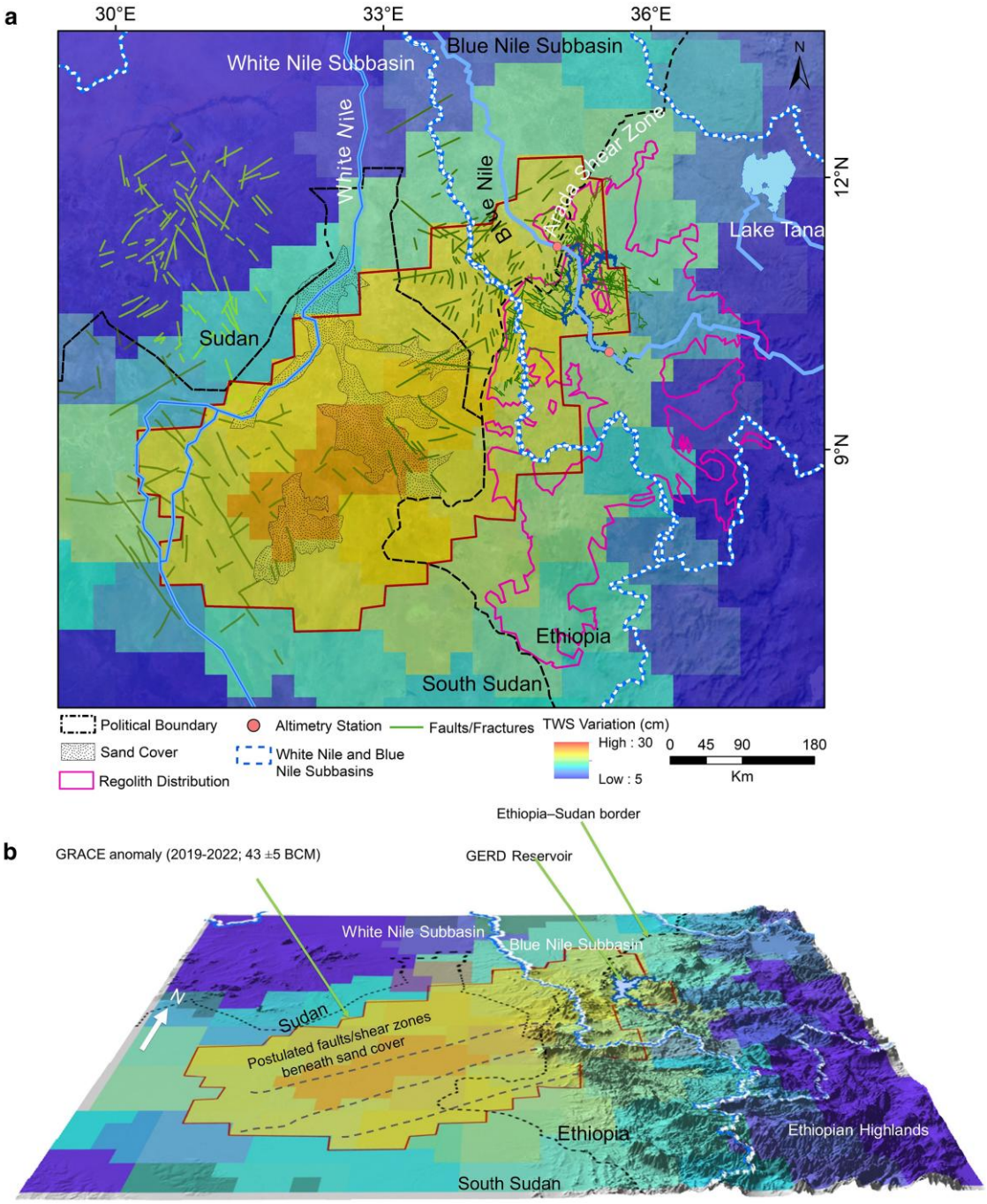

Fig. 6. The spatial and temporal increase in $GRACE_{TWS}$ over the GERD and its surroundings throughout the filling years. a) A $GRACE_{TWS}$ seasonal peak difference product generated by subtracting the maximum seasonal $GRACE_{TWS}$ for 2019 from that of 2022; the figure shows an anomaly portraying an increase in mass extending from the GERD construction site in the Ethiopian Highlands in a southwest direction for some 300 km along faults/shear zone complex within the Ethiopian Highlands and their projected extension in Sudan toward the lowlands in South Sudan, where the maximum $GRACE_{TWS}$ values are observed. b) A 3D representation of a.

The cited lines of evidence have limitations. Uncertainties in the estimated $GRACE_{TWS}$ could arise from assuming that the temporal mass variations in the difference product are related solely to variations in the volume of impounded waters and seepage from the reservoir and ignoring potential contributions from precipitation. Uncertainties in the daily mass balance calculations arise from the absence of measured inflow data due to restrictions imposed by the upstream country on publishing the data and from extracting the daily inflow and the change in reservoir storage by interpolating satellite (Sentinel-1 radar and altimeter) acquisitions weeks apart. In our daily seepage and gain values calculations, we assumed that the inflow was equal to the outflow at Eldiem station before filling the GERD reservoir (2009–2019). This assumption can introduce additional, unaccounted-for uncertainties as the stream might be gaining or losing water between the inflow and outflow stations. It will fictitiously increase the estimated inflow for a gaining stream and vice versa for a losing stream. We acknowledge those limitations but argue that the estimated seepage value (19.8 ± 6 BCM) is robust, given the similarity of the estimated seepage from three independent methods.

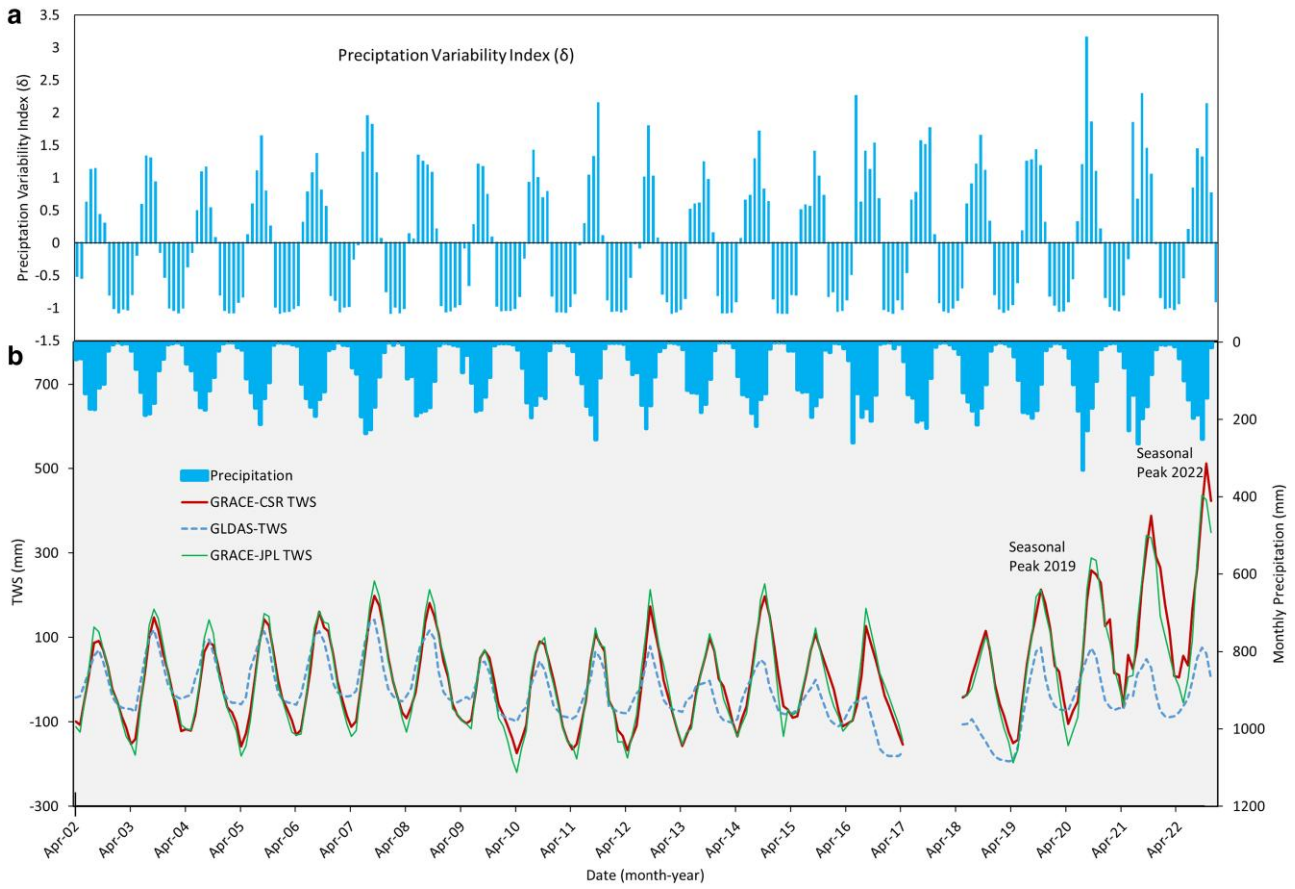

Fig. 7. Precipitation, precipitation variability index, $GRACE_{TWS}$, and GLDAS time series (2002–2023) over the anomaly in Figure 6. a) Precipitation variability index (δ) time series. b) Comparison between monthly $GRACE_{TWS}$ mascon (CSR and JPL), $GLDAS_{TWS}$, and precipitation (extracted from CHIRPS) time series. The seasonal peaks for 2019 and 2022, from which the $GRACE_{TWS}$ seasonal peak difference product was generated, are labeled.

We recognize that additional field, geophysical, and geochemical data are needed to refine the seepage estimates presented in this work.

The present study provides three independent and consistent estimates of GERD seepage, which has been vastly underestimated or ignored in water management scenarios (6, 34, 35). Previous studies assumed that seepage, if it occurs, would ultimately return to the Nile River course downstream of the GERD (6, 36). This assumption would have been valid if we did not have densely distributed, deep-seated fault networks flooring the GERD reservoir, extending across the basement terrains in Western Ethiopia and connecting several catchments across the topographic divides (Fig. 1). Inter-catchment groundwater flow through faults and fractures at the scale of the headwaters can make up a relatively large proportion of the water balance amounting to 10 % of mean AP on the average (37).

Recommendations and conclusions

Overlooking the significant seepage from the GERD would result in inappropriate water management policies across the Nile River riparian countries and adversely impact future negotiations on the GERD filling and operations. The estimated significant losses to seepage over the first three years of the GERD filling are at odds with many of the hydrological models that assess filling and management scenarios, water allocations, and the socioeconomic impacts on downstream countries; they also raise concerns about the effectiveness of these models in sustaining resilient water strategies for the Nile Basin. Our results suggest that ongoing negotiation on water allocation and management under different climatic (i.e. dry, average, and wet) conditions over the Nile Basin should no longer overlook the seepage rates from the major Nile Basin reservoirs (i.e. Aswan High Dam and GERD). If adopted, our suggestions could potentially contribute to establishing well-informed collaborative agreements and resilient water strategies between the Nile Basin countries based on balanced and comprehensive hydrological models.

We recommend developing comprehensive continuous monitoring systems for the GERD, including stream flow (inflow and outflow), groundwater levels, and reservoir surface WLs. In the absence of such systems, we recommend applying the approaches presented in this work throughout the remaining filling years and beyond. The ground or satellite-based monitoring systems will validate our interpretations and enhance our understanding of the long-term impacts of GERD on the downstream countries. For example, as the filling proceeds, the impounded waters will cover new areas and access additional highly fractured terrains such as the N–S trending Arada, Mankusha, and Babizenda shear zones in the north, the E–W-trending Omedla shear in the east, and the karstified calcite limestones in the south (Fig. 2), all of which could represent preferred pathways for groundwater flow away from the GERD reservoir. On the other hand, monitoring could reveal a progressive decrease in seepage with time, as with Lake Nasser. Using a two-dimensional groundwater flow model for Lake Nasser and its surroundings, calibrated

Table 1. Maximum WL and WV attained during years I, II, and III and minimum WL and WV following the fillings extracted from CDEM and temporal Sentinel-1 radar data.

Year	Max WL (m)	Max WV (BCM)	Area (km^2)	Min WL (m)	Min WV (BCM)	ΔWL (m)	ΔWV (BCM)	Evaporation (BCM)
I	566	4.3 ± 0.2	207	560	2.6 ± 0.1	6	1.7 ± 0.1	0.8 ± 0.2
II	580	9.3 ± 0.1	379	574	5.8 ± 0.1	6	3.50 ± 0.04	1.2 ± 0.4
III	606	26.8 ± 1.5	841	600	19.9 ± 1.2	6	6.9 ± 0.4	1.4 ± 0.4

Area: The areal extent of the reservoir (km^2), the area occupied by the darkest pixels on Sentinel-1 radar images.
WL: Surface water level of the reservoir (m.a.m.s.l) extracted from CDEM and Sentinel-1 data.
WV: Water volume in the reservoir (BCM) extracted from CDEM and Sentinel-1 data.
Evaporation: Estimated losses to evaporation during the operation of the GERD (2020–2022), taking into consideration the seasonal variations in evaporation rates (31) and the temporal variations in the reservoir areal extent.

against head data (38), found that the seepage decreased by 15–20% each year (1996, 7.4 km^3; 2001, 2.7 km^3) due to the gradual reduction in hydraulic gradient between the lake stage and the groundwater level and possibly due to the sealing of the fracture and fault networks by the silts and clays carried by waters leaving the reservoir.

During the past two decades, many satellite-based sensors have been deployed to monitor the anthropogenic and natural contributions to hydrologic systems across the globe. Of equal importance is the availability of these data at no cost to the scientific community. Applications similar to those described here are helpful, especially in inaccessible areas and in others where data sharing is absent or limited. They are not a substitute for traditional methods.

Materials and methods

Digital elevation

A high-resolution (2.5 m) digital terrain model (DTM) was generated from a set of stereo panchromatic SPOT-6/7 imagery. ENVI photogrammetry and LIDAR modules were used to create point cloud data from stereo images and extract DTM from the point cloud data, respectively. Ten images collected between 2015 and 2020 during the dry seasons (December–April) when the river level was at its minimum were selected to improve the coverage around the river channel. The point cloud was generated using the dense image matching method. The point cloud data were further processed to extract a high-resolution (2.5 m) DTM by refining the point cloud and removing the points associated with the tree canopy. The generated DTM was used to extract channel profiles.

Copernicus digital elevation model (CDEM) is an open-access DEM provided by the European Space Agency with global coverage at a 30-m resolution. The DEM was downloaded from (https://spacedata.copernicus.eu/collections/copernicus-digital-elevation-model/) and used to delineate the stream network and watershed boundaries over the entire GERD reservoir and surroundings areas using ArcGIS version 10.8 hydrological tools (https://www.arcgis.com/). The DEM was also used to estimate the temporal variations in the reservoir's water storage and generate 3D views of the GRACE difference maps. The $GRACE_{TWS}$ anomaly was draped over the terrain surface of the TIN layer (irregular triangular network) using the 3D Analyst and ArcScene tools, enabling a 3D view of the surface topography (https://www.arcgis.com/).

Precipitation

The temporal variation in precipitation over the GERD was extracted from the Climate Hazards Center InfraRed Precipitation with Station (CHIRPS) precipitation dataset (39). The CHIRPS precipitation data exhibited the best correlation with the rain gauge stations in the Blue Nile region (18). The CHIRPS precipitation dataset represents progress from earlier techniques that relied on interpolation methods and infrared conventional charge-coupled device observations to obtain high-resolution precipitation estimates. The data integrate satellite imagery with in situ station data with a resolution of 0.05° over 30 years (39). The CHIRPS version 2.0 Final, which provides monthly data, is used in this study. The data are available at (https://data.apps.fao.org/catalog/organization/chirps). Utilizing this dataset, we calculated the precipitation variability index (δ) using Eq. 1 for 2002–2022 (40, 41). This index distinguishes between drought (indicated by negative δ values) and wet years (indicated by positive δ values), providing a nuanced understanding of hydrological variability in the study area.

$$\delta_i = (P_i - \mu)/\sigma \quad \text{(Eq.1)}$$

where δ_i is the precipitation variability index for a month (i), P_i is the monthly precipitation (i), and μ and σ are the average and the SD of the precipitation throughout the entire period 2002–2022, respectively.

Sentinel-1 radar images and radar altimetry

The Sentinel-1A/B ground range detected radar scenes were collected in Interferometric Wide (IW) mode with 10 m pixel spacing (69 scenes from July 2020 to December 2022) in ascending and descending orbital geometries. Each image was processed in the Google Earth Engine platform to generate a single-band vertical transmit/vertical receive (VV) (single co-polarization) image. The backscattering coefficient (σ unit: decibels [dB]) was estimated from the band values. Pixels with σ_{VV} values <–18 dB were identified as water pixels (42). Using those images and thresholds, we mapped the temporal variations in the areal extent of the reservoir throughout the filling years.

We extracted the time series for surface WLs from the Database for Hydrological Time Series of Inland Waters (DAHITI). The WL time series were extracted from 30 measurements for the downstream station and 81 for the upstream station (Fig. 4). The repository offers WL time-series data from three types of multimission satellite radar altimetry (43). Those are the Sentinel-3A [LR, v2], the Jason-3 [IGDR-F], and the Jason-2 [SGDR-D]. The reported uncertainties in WL measurement from radar altimetry are those provided by the DAHITI.

Mass balance calculations

Mass balance calculations involved multiple steps: (i) extraction of temporal variations in reservoir volume and accounting for the associated losses due to evaporation over time, (ii) extraction of temporal variations on inflow and outflow to the GERD in the filling years, and (iii) estimation of losses to seepage using mass balance calculations.

Extraction of temporal variations in reservoir volume

We estimated the lake storage by delineating the areal extent of the reservoir using Sentinel-1 radar time series (69 images), the area occupied by the darkest pixels on the image (Extend Data Fig. 3). Then, we identified the WL corresponding to the delineated areal extent. Specifically, we selected the DEM contour defining the extracted areal extent. Finally, we estimated the volume of water in the lake at any time from the volume subtended by the horizontal plane containing the identified contour and the DEM defining the surface elevation of the lake bottom and sides. The uncertainty in the reported volumes (Table 1) was estimated from the differences between the estimated volumes for each of fillings I, II, and III that were derived using two separate DEMS, the CDEM, and Advanced Land Observing Satellite (ALOS) DEM.

We estimated daily temporal variations in reservoir storage and evaporation rates to conduct WMB calculations daily. We calculated the daily deviations in lake storage from the volumes extracted from the individual Sentinel-1 images (69 images) and applied linear interpolation methods to fill the gaps between the available Sentinel-1 images.

Several studies have been conducted to estimate the evaporation rates of the GERD reservoir (6, 44–46). Using evaporation rates reported in those three studies, we calculated the total evaporation losses during the operation of the GERD (2020–2022) at 4.25, 3.4, and 2.1 BCM, respectively. In our mass balance calculations, we adopted the median evaporation rates and losses (total losses to evaporation: 3.4 BCM). We estimated the uncertainty in the total losses to evaporation from the SD of the three estimates.

Extraction of temporal variations in the inflow to and outflow from the GERD during the filling years

Stream gauging data are publicly available downstream of the GERD (Eldiem station; Fig. 1) but not in its upstream. Using two methods, we estimated the temporal variations in the river flow rate (Q) upstream of the GERD. The first method (Method I) involved the following steps: (i) extracting surface WLs over the radar altimetry upstream location (Fig. 1); (ii) measuring river cross-sectional area using ArcGIS 3D Analyst Tool from 2.5-m resolution DEM extracted from ten high-resolution (1 m) winter SPOT scenes (Supplementary Fig. S3); (iii) deriving geometric values of trapezoidal form that best fit the channel cross section (i.e. width and side slope of the channel and elevation of its bottom); (iv) calibrating the parameters of Manning's equation (e.g. roughness coefficient and depth-dependent hydraulic radius and cross-sectional area) against the historical streamflow measured before dam filling using performance criteria of NSE and KGE assuming three possible forms (trapezoidal, parabolic, and triangular) that extend below the elevation of the observed channel bottom with an unknown depth (Section 6 in the Supplementary file); and (v) estimating river flow rate (Q) over the station for each of the extracted WL using a calibrated Manning's equation (Eq. 2):

$$Q = \left(\frac{1}{n}\right) A R^{2/3} \sqrt{S} \qquad \text{(Eq.2)}$$

$$R = \frac{A}{P} \qquad \text{(Eq.3)}$$

where A is the flow cross-sectional area (m^2), n is the Manning's roughness coefficient, R is the hydraulic radius (m), S is the channel slope (m/m), and P is the wetted perimeter. We used a slope of 0.004 measured using the ArcGIS 3D Analyst Tool. The equation was calibrated by optimizing both *n* with a range of 0.02–0.07, which is typical for natural river channels (47), and depth, which governs A, P, and R based on three possible channel forms below the observed channel bottom (Section 5 in the Supplementary file). All three forms achieved high performance, yet the trapezoidal shape was slightly better than the other two based on the combined score of NSE (0.903) and KGE (0.929). Both NSE and KGE are commonly used as performance measures for hydrologic models (48). The optimum parameters were $n = 0.07$, depth = 1.52 m below the observed channel bottom, and a trapezoidal shape extending above and below the observed channel bottom.

In the second method (Method II), we used the measured daily outflow data in the Eldiem station at the downstream location to estimate the inflow rate upstream. We first assumed that the inflow was equal to the outflow at Eldiem station before filling the GERD (2009–2019). The radar altimetry data (water elevation upstream) and measured outflow (Eldiem station) were randomly partitioned into two groups: training dataset (80%) and testing dataset (20%) using the Random Package in R-statistics. We used the training data to derive a second-degree polynomial relationship between upstream water elevation and measured outflow (Section 6 in the Supplementary file). The relationship was then evaluated (NSE: 0.8; RMSE: 0.12) by comparing the predicted outflow at the Eldiem station against measured values (Section 6 in the Supplementary file), indicating the model's robustness.

We derived a polynomial (second) relationship between the radar altimetry elevation over the upstream station (Fig. 1) and the measured outflow at Eldiem station (49) from 2009 to 2019. Then, we used the derived relationship (Eqs. 4 and 5) to estimate the upstream inflow rate (inflow) during the operation period of the GERD (2020–2022) (Supplementary Figure S5).

$$\text{Inflow}\ (t) = a \times WL(t)^2 + b \times WL(t) + c \qquad \text{(Eq.4)}$$

$$\text{Inflow}\ (t) = 2.4239\ WL(t)^2 - 2870.1 \times WL(t) + 848805 \qquad \text{(Eq.5)}$$

where inflow (t) is the inflow at time (t), WL(t) is the radar altimetry elevation over the upstream station at time (t), and a, b, and c represent the constants of quadratic coefficients.

Estimating losses to seepage using mass balance calculations

The following mass balance equation governs the partitioning of runoff in and out of the GERD:

$$\text{Inflow} = \text{Outflow} + \Delta WV + \text{Evaporation} \qquad \text{(Eq.6)}$$

where the daily inflow equals the daily outflow plus the daily change in reservoir storage (WV) and evaporation losses.

Rearranging Eq. 6 gives:

$$\text{Inflow} - \text{Outflow} - \Delta WV - \text{Evaporation} = 0 \qquad \text{(Eq.7)}$$

We applied Eq. 7 to extract daily seepage or gains to the system, where + ve values indicate losses to seepage and –ve values gains from the base flow.

The uncertainty (σ) in WMB was calculated by adding, in quadrature, errors related to inflow, outflow, evaporation, and ΔWV (Eq. 8). We used the reported temporal errors for the radar altimetry data in the upstream station (DAHITI) to extract the corresponding temporal errors in inflow from Methods I and II. In Method I, we incorporated the reported temporal errors from radar altimetry into a randomly selected subset (213 of 853 samples; 25%) of WLs using R statistics. We then calculated the corresponding daily inflow values for the subset dataset using Eq. 2. We estimated the uncertainty in the inflow values from the difference between the original (error-inclusive inflow data) and subset

inflow datasets (error-exclusive inflow data). We used a similar method to estimate the uncertainty in the inflow values using Method II by incorporating the altimetry errors into the entire WL dataset. We then calculated the corresponding daily inflow values using Eq. 4 and estimated the uncertainty in the inflow values from the difference between the original and modified inflow values. The uncertainty for the measured outflow data at the Eldiem gauge station was assumed to be negligible (σoutflow = 0).

$$\sigma WMB = \sqrt{\sigma inflow^2 + \sigma outflow^2 + \sigma \Delta WV^2 + \sigma Evap.^2} \qquad \text{(Eq.8)}$$

GRACE and GRACE-FO

We use the GRACE and GRACE-FO solutions to calculate the temporal variation in storage ($GRACE_{TWS}$) over the reservoir and its surroundings. We used two solutions from GRACE–GRACE-FO missions. Those are the mascon solution from the Jet Propulsion Laboratory (JPL RL06.1M-CRI) and the mascon solution from the Center of Space Research in Texas (CSR-RL06M) (31, 50–53). The average of the two GRACE solutions was used to extract and report the temporal variation in TWS over the GERD (33, 54, 55). Still, the individual solutions were used for display purposes (e.g. Fig. 6). The difference in storage volumes extracted from JPL RL06.1M-CRI and CSR-RL06M represented the uncertainty in the reported TWS variation (54, 56).

We constructed a difference product between the seasonal peak (annual maximum) of $GRACE_{TWS}$ values for 2022 and 2019 (Fig. 6a) and draped it over topography (Fig. 6b). We used the difference product to identify and display the spatial and temporal increase in $GRACE_{TWS}$ over the GERD and its surroundings throughout the filling years and to reveal groundwater migration patterns. 2019 is the year preceding the construction of the GERD, and 2022 is the third year of filling.

The monthly mean values were calculated at GRACE and GRACE-FO monthly time steps after subtracting the climatology mean from 2005 to 2009 (57, 58). We compared the $GRACE_{TWS}$ time series to simulated monthly TWS derived from GLDAS (Fig. 7) to identify periods where anthropogenic contributions affected GRACE solutions. The former ($GRACE_{TWS}$) measures the natural and anthropogenic contributions, whereas the latter estimates the natural contributions only.

Acknowledgments

The authors thank the PNAS reviewers for their instructive comments and suggestions.

Supplementary Material

Supplementary material is available at *PNAS Nexus* online.

Funding

Funding was provided by the National Aeronautics and Space Administration (NASA) Earth Science Division grant 80NSSC20K0767 and 80NSSC24K1155 awarded to Western Michigan University.

Author Contributions

K.A., M.S., E.Y., and H.S. conceived and conceptualized the study. K.A., M.S., E.Y., and H.E. processed and analyzed the data and extracted the findings. K.A., M.S., and A.Z.A. wrote the manuscript. M.S., K.A., A.Z.A., H.E., K. Abdelmalik, and E.Y. contributed to and reviewed the manuscript.

Data Availability

Publicly available datasets include stream discharge, radar altimetry, GRACE, Sentinel images, Landsat images, and DEMs. The archived data portals for these datasets are provided in the Reference section, facilitating easy access for further research and analysis. All processed datasets aggregated to the study area have been deposited in figshare at https://doi.org/10.6084/m9.figshare.25903777. GIS Feature structure layer https://gis.acaciadata.com/?map=/project/gw4e/gw4e.qgz&service=WMS&request=GetCapabilities&

References

1 Dumont HJ. 2009. A description of the Nile Basin, and a synopsis of its history, ecology, biogeography, hydrology, and natural resources. In: Dumont HJ, editor. The Nile. Monographiae Biologicae, vol. 89. Dordrecht: Springer. https://doi.org/10.1007/978-1-4020-9726-3_1.

2 Melesse AM, Weng Q, Thenkabail PS, Senay GB. 2007. Remote sensing sensors and applications in environmental resources mapping and modelling. *Sensors*. 7:3209–3241.

3 (FAO) Food and Agriculture Organization of the United Nations. 2015. Water Development and Management Unit. *CLIMWAT2.0; 1*, https://www.fao.org/land-water/databases-and-software/climwat-for-cropwat/en/.

4 Malede DA, Agumassie TA, Kosgei JR, Linh NTT, Andualem TG. 2022. Analysis of rainfall and streamflow trend and variability over Birr River watershed, Abbay basin, Ethiopia. *Environ Challenges*. 7:100528.

5 Chen H, Swain A. 2014. The Grand Ethiopian Renaissance Dam: evaluating its sustainability standard and geopolitical significance. *Energy Dev Front*. 3:11–19.

6 Wheeler KG, Jeuland M, Hall JW, Zagona E, Whittington D. 2020. Understanding and managing new risks on the Nile with the Grand Ethiopian Renaissance Dam. *Nat Commun*. 11(1):5222. https://doi.org/10.1038/s41467-020-19089-x.

7 Wheeler KG, *et al.* 2016. Cooperative filling approaches for the Grand Ethiopian Renaissance Dam. *Water Int*. 41:611–634. https://doi.org/10.1080/02508060.2016.1177698.

8 Liersch S, Koch H, Hattermann FF. 2017. Management scenarios of the Grand Ethiopian Renaissance Dam and their impacts under recent and future climates. *Water (Basel)*. 9:728–729.

9 Eldardiry H, Hossain F. 2021. A blueprint for adapting high Aswan dam operation in Egypt to challenges of filling and operation of the Grand Ethiopian Renaissance dam. *J. Hydrol*. 598:125708. https://doi.org/10.1016/j.jhydrol.2020.125708.

10 Heggy E, Sharkawy Z, Abotalib AZ. 2021. Egypt's water budget deficit and suggested mitigation policies for the Grand Ethiopian Renaissance Dam filling scenarios. *Environ Res Lett*. 16:074022. https://doi.org/10.1088/1748-9326/ac0ac9.

11 Sterl S, Fadly D, Liersch S, Koch H, Thiery W. 2021. Linking solar and wind power in eastern Africa with operation of the Grand Ethiopian Renaissance Dam. *Nat Energy*. 64(6):407–418. https://doi.org/10.1038/s41560-021-00799-5.

12 Basheer M, *et al.* 2023. Negotiating Nile infrastructure management should consider climate change uncertainties. *Nat Clim Chang*. 131(13):17–19.

13 Elagib NA, Basheer M. 2021. Would Africa's largest hydropower dam have profound environmental impacts? Environ. *Sci Pollut Res*. 28:8936–8944.

14 Abotalib AZ, *et al.* 2023. Irreversible and large-scale heavy metal pollution arising from increased damming and untreated water reuse in the Nile Delta. *Earth's Futur*. 11:e2022EF002987.

15 Mahmoud MR, Fahmy H, Garcia LA. 2022. Potential impacts of failure of the Grand Ethiopian Renaissance Dam on downstream countries. *J Flood Risk Manag*. 15:e12793.

16 Eldeeb HM, *et al.* 2023. Assessment of dams' failure and flood wave hazards on the downstream countries: a case study of the Grand Ethiopian Renaissance Dam (GERD). *Water (Basel)*. 15: 1609.

17 Elganainy MA, Eldwer AE. 2018. Stochastic forecasting models of the monthly streamflow for the Blue Nile at Eldiem station. *Water Resour*. 45:326–337.

18 Ali AM, Melsen LA, Teuling AJ. 2023. Inferring reservoir filling strategies under limiteddata availability conditions using hydrological modeling and Earth observations: the case of the Grand Ethiopian Renaissance Dam (GERD). *Hydrol Earth Syst Sci*. 7(21). https://doi.org/10.5194/hess-27-4057-2023.

19 Lazin R, Shen X, Moges S, Anagnostou E. 2023. The role of renaissance dam in reducing hydrological extremes in the Upper Blue Nile Basin: current and future climate scenarios. *J Hydrol*. 616: 128753.

20 Digna RF, *et al.* 2018. Impact of water resources development on water availability for hydropower production and irrigated agriculture of the eastern Nile Basin. *J Water Resour Plan Manag*. 144: 05018007.

21 Groen J, *et al.* 2020. Groundwater mapping for climate resilient WASH in arid and semi-arid areas of Ethiopia. *GW4E Project Summary Report*. https://en.acaciawater.com/nw-29143-7-3814949/nieuws/groundwater_mapping_for_climate_resilient_wash_in_ethiopia.html.

22 Gani ND, Abdelsalam MG, Gera S, Gani MR. 2009. Stratigraphic and structural evolution of the Blue Nile Basin, northwestern Ethiopian plateau. *Geol J*. 44:30–56.

23 Dow DB, Beyth M, Hailu T. 1971. Palaeozoic glacial rocks recently discovered in northern Ethiopia. *Geol Mag*. 108:53–60.

24 Mohamed M, Elmahdy S. 2017. Remote sensing of the Grand Ethiopian Renaissance Dam: a hazard and environmental impacts assessment. *Geomatics Nat Hazards Risk*. 8:1225–1240.

25 GSE. Geological Map of Ethiopia by Geological Survey of Ethiopia, sheets NC36–8 and NC36-7, Scale 1:250,000. 2004. https://shop.geospatial.com/publication/N489H9H20A8GMZ61HB4KQW2M82/Ethiopia-1-to-250000-Scale-Geological-Maps.

26 GMRD, Geological and Mineral Resources Department of Sudan. 1981. Geological Map of the Sudan, scale 1: 2,000,000. https://esdac.jrc.ec.europa.eu/content/geological-map-sudan.

27 GSE. Geological Map of Ethiopia by Geological Survey of Ethiopia, sheets NC36-4, Scale 1:250,000. 1997. https://shop.geospatial.com/publication/N489H9H20A8GMZ61HB4KQW2M82/Ethiopia-1-to-250000-Scale-Geological-Maps.

28 Deyassa G, Kebede S, Ayenew T, Kidane T. 2014. Crystalline basement aquifers of Ethiopia: their genesis, classification and aquifer properties. *J African Earth Sci*. 100:191–202.

29 Tesemma ZK, Mohamed YA, Steenhuis TS. 2010. Trends in rainfall and runoff in the Blue Nile Basin: 1964–2003. *Hydrol Process*. 24:3747–3758.

30 Kebede M, Kanninen M, Yirdaw E, Lemenih M. 2013. Vegetation structural characteristics and topographic factors in the remnant moist Afromontane forest of Wondo Genet, south central Ethiopia. *J For Res*. 24:419–430.

31 Save H, Bettadpur S, Tapley BD. 2016. High-resolution CSR GRACE RL05 mascons. *J Geophys Res Solid Earth*. 121:7547–7569.

32 Tapley BD, Bettadpur S, Watkins M, Reigber C. 2004. The gravity recovery and climate experiment: mission overview and early results. *Geophys Res Lett*. 31:L09607.

33 Abdelmohsen K, Sultan M, Save H, Abotalib AZ, Yan E. 2020. What can the GRACE seasonal cycle tell us about lake-aquifer interactions? *Earth Sci Rev*. 211:103392.

34 Eldardiry H, Hossain F. 2021. The value of long-term streamflow forecasts in adaptive reservoir operation: the case of the High Aswan dam in the transboundary Nile River basin. *J Hydrometeorol*. 22:1099–1115.

35 Basheer M, *et al.* 2023. Cooperative adaptive management of the Nile River with climate and socio-economic uncertainties. *Nat Clim Chang*. 131(13):48–57.

36 Wheeler K, *et al.* 2022. Comment on 'Egypt's water budget deficit and suggested mitigation policies for the Grand Ethiopian Renaissance Dam filling scenarios.' *Environ Res Lett*. 17:088003.

37 Bouaziz L, *et al.* 2018. Redressing the balance: quantifying net intercatchment groundwater flows. *Hydrol Earth Syst Sci*. 22:6415–6434.

38 Sultan M, *et al.* 2013. Assessment of the vulnerabilities of the Nubian Sandstone Fossil Aquifer, North Africa. *Climate Vulnerability*. 5:311–333. https://doi.org/10.1016/B978-0-12-384703-4.00531-1.

39 Funk C, *et al.* 2015. The climate hazards infrared precipitation with stations—a new environmental record for monitoring extremes. *Sci Data*. 2:150066.

40 Gocic M, Trajkovic S. 2013. Analysis of precipitation and drought data in Serbia over the period 1980–2010. *J Hydrol*. 494:32–42.

41 Abdelmohsen K, *et al.* 2022. Buffering the impacts of extreme climate variability in the highly engineered Tigris Euphrates river system. *Sci Rep*. 12:4178.

42 Abou Samra RM, Ali RR. 2021. Detection of the filling phases of the Grand Ethiopian Renaissance dam using sentinel-1 SAR data. *Egypt J Remote Sens Sp Sci*. 24:991–997.

43 Schwatke C, Dettmering D, Bosch W, Seitz F. 2015. DAHITI an innovative approach for estimating water level time series over inland waters using multi-mission satellite altimetry. *Hydrol Earth Syst Sci*. 19:4345–4364.

44 Adem AA, Aynalem DW, Tilahun SA, Steenhuis TS. 2017. Predicting reference evaporation for the Ethiopian highlands. *J Water Resour Prot*. 9:1244–1269.

45 Hordofa T. 2003. Modelling of evaporation over Ethiopia. *Agric Eng Irrig Water Manag Eng*. http://krishikosh.egranth.ac.in/handle/1/5810013077.

46 AbuZeid KM. 2021. Potential transboundary impacts of the grand Ethiopian renaissance dam under climate change and variability. In: Diop S, Scheren P, Niang A, editors. Climate change and water resources in Africa. Cham: Springer. https://doi.org/10.1007/978-3-030-61225-2_16.

47 Chow VT. 1959. *Open-channel hydraulics*. New York: McGraw-Hill B. Co. p. 680P.

48 Knoben WJM, Freer JE, Woods RA. 2019. Technical note: inherent benchmark or not? Comparing Nash-Sutcliffe and Kling-Gupta efficiency scores. *Hydrol Earth Syst Sci*. 23:4323–4331.

49 Hansson M. 2013. Rating of discharge at monitoring station affected by backwater effects—El Deim Station in the Blue Nile. Department of Earth Sciences, Program for Air, Water and Landscape Sciences. http://www.diva-portal.se/smash/get/diva2:643838/FULLTEXT01.pdf.

50 Save Himanshu. 2019. CSR GRACE RL06 Mascon Solutions. *Texas Data Repository*. v1. https://doi.org/10.18738/T8/UN91VR.

51 Watkins MM, Wiese DN, Yuan DN, Boening C, Landerer FW. 2015. Improved methods for observing Earth's time variable mass distribution with GRACE using spherical cap mascons. *J Geophys Res B Solid Earth*. 120:2648–2671.

52 Wiese D, Landerer FW, Watkins MM. 2016. Quantifying and reducing leakage errors in the JPL RL05M GRACE mascon solution. *Water Resour Res*. 52:7490–7502.

53 Loomis BD, Luthcke SB, Sabaka TJ. 2019. Regularization and error characterization of GRACE mascons. *J Geod*. 93: 1381–1398.

54 Rodell M, *et al.* 2018. Emerging trends in global freshwater availability. *Nature*. 557:651–659. https://doi.org/10.1038/s41586-018-0123-1

55 Abdelmohsen K, *et al.* 2019. Response of deep aquifers to climate variability. *Sci Total Environ*. 677:530–544.

56 Scanlon BR, *et al.* 2018. Global models underestimate large decadal declining and rising water storage trends relative to GRACE satellite data. *Proceedings of the National Academy of Sciences of the United States of America*. 115(6). https://doi.org/10.1073/pnas.1704665115.

57 Landerer FW, Swenson SC. 2012. Accuracy of scaled GRACE terrestrial water storage estimates. *Water Resour Res*. 48:4531.

58 Rodell M, *et al.* 2020. Monthly gridded Global Land Data Assimilation System (GLDAS) from Noah-v3.3 land hydrology model for GRACE and GRACE-FO over nominal months. PO.DAAC, CA, USA. https://doi.org/10.5067/GGDAS-3NH33.